Fundamental Limits on Measuring the Rotational Constraint of Single Molecules using Fluorescence Microscopy

Oumeng Zhang and Matthew D. Lew*
Department of Electrical and Systems Engineering, Washington University in St. Louis, Missouri 63130, USA
(Dated: November 26, 2018)

Optical fluorescence imaging is capable of measuring both the spatial and rotational dynamics of single molecules. However, unavoidable measurement noise will result in inaccurate estimates of rotational dynamics, causing a molecule to appear to be more rotationally constrained than it actually is. We report a mathematical framework to compute the fundamental limit of accuracy in measuring the rotational mobility of dipole-like emitters. By applying our framework to both in-plane and three-dimensional methods, we provide a means to choose the optimal orientation-measurement technique based on experimental conditions.

Fluorescence microscopy has been widely utilized to study the rotational dynamics of single molecules (SMs), revealing new insights into DNA organization [1–3] and the movement of molecular motors [4–8]. Orientation measurements are also critical for ensuring the accuracy of SM localization microscopy [9–12], since changes in orientation can be mistakenly perceived as changes in molecular position. To sensitively measure dipole orientation, a fluorescence microscope is typically augmented either by measuring fluorescence emission under varying pumping polarization, by manipulating the polarization and/or angular spectrum of the fluorescence emission, or both [13]. Analyzing an SM's fluorescence signal thereby yields its average orientation and/or its rotational mobility or "wobble" during some integration time.

One intuitive method to measure SM orientation is to quantify linear dichroism (LD) [14–17], i.e., the ratio of the difference over the sum of the intensity of the x- and y-polarized emission from a single emitter. A rotationally-fixed SM will yield a certain LD value depending upon its orientation, but due to symmetry, a rotationally-unconstrained SM will give an LD of zero. However, measurement noise, e.g., photon shot noise, unavoidably complicates the interpretation of these measurements, since any finite number of photons will almost certainly produce a nonzero LD and therefore reduce the apparent molecular wobble. This phenomena is similar to the effect of finite localization precision in single-particle tracking [18–22], where a translationally-fixed particle appears to have a nonzero diffusion coefficient due to shot noise. However, in the case of rotational dynamics, the non-zero estimates of LD cause the measurement of rotational mobility to be biased; the molecule will appear to be *more constrained* than it actually is. To our knowledge, the effects of noise and measurement sensitivity and the impact of 2D versus 3D measurements on the accuracy of quantifying SM rotational dynamics remains unexplored.

Here, we present a mathematical framework to compute the distribution, accuracy, and precision of measuring the rotational constraint (inversely proportional to rotational mobility) of dipole-like emitters in both 2D and 3D. For a given imaging scenario with a certain number of signal and background photons detected, we derive a lower bound on the apparent rotational constraint, that is, the expectation of estimated rotational constraint for a freely-rotating molecule; it is impossible to detect a constraint smaller than this limit. Further, we derive a relation between the measured in (xy)-plane and 3D rotational constraints, which reveals how 2D and 3D methods perceive the same 3D rotational diffusion differently. We then analyze the accuracy and precision of various commonly-used and state-of-the-art 2D and 3D orientation measurement techniques.

We model a fluorescent molecule as a dipole with orientation $\boldsymbol{\mu} = [\mu_x, \mu_y, \mu_z]^\dagger$ in Cartesian coordinates, where μ_z is the out-of-plane component, i.e., the projection of $\boldsymbol{\mu}$ along the optical axis. Since fluorescence intensity and not electric field is detected, both excitation and emission modulation methods are limited to measuring the even-order moments of $\boldsymbol{\mu}$. The recorded image $\boldsymbol{g}$ can then be represented using the second moments of $\boldsymbol{\mu}$, given by

$$\boldsymbol{g} = s[\boldsymbol{B}_{xx}, \boldsymbol{B}_{yy}, \boldsymbol{B}_{zz}, \boldsymbol{B}_{xy}, \boldsymbol{B}_{xz}, \boldsymbol{B}_{yz}] \\ [\langle\mu_x^2\rangle, \langle\mu_y^2\rangle, \langle\mu_z^2\rangle, \langle\mu_x\mu_y\rangle, \langle\mu_x\mu_z\rangle, \langle\mu_y\mu_z\rangle]^\dagger + \boldsymbol{b} \quad (1)$$

for a 3D measurement and

$$\boldsymbol{g} = s[\boldsymbol{B}_{xx}, \boldsymbol{B}_{yy}, \boldsymbol{B}_{xy}][\langle\zeta_x^2\rangle, \langle\zeta_y^2\rangle, \langle\zeta_x\zeta_y\rangle]^\dagger + \boldsymbol{b} \quad (2)$$

for an in-plane (2D) measurement, where $\boldsymbol{B}_{ij}$ are termed the basis images of the imaging system, that is, the image produced by an emitter exhibiting orientational second moment $\langle\mu_i\mu_j\rangle$. The prefactor s and image $\boldsymbol{b} = [b_1, ..., b_n]$ represent the integrated signal photons and background photons for each measurement $\boldsymbol{g}$ respectively. The second moment vector $\boldsymbol{\zeta} = [\zeta_x, \zeta_y]^\dagger = [\mu_x, \mu_y]^\dagger / \sqrt{\mu_x^2 + \mu_y^2}$ is the normalized projection of molecular orientation $\boldsymbol{\mu}$ into the xy plane, and the angle brackets $\langle\cdot\rangle$ denote the temporal average taken over one camera frame or the equivalent average over the orientation domain. The basis images can be computed for any excitation modulation method

by computing the SM's response to varying excitation polarization [3] and for any emission modulation technique using vectorial diffraction models [23–27].

The accuracy and precision with which the rotational constraint of a single molecule can be estimated depend on three factors: 1) the detected photons from the emitter, i.e., its signal, 2) background fluorescence, and 3) most importantly, the basis-image matrix that describes the sensitivity of the imaging system to each orientational second moment $\langle \mu_i \mu_j \rangle$. To illustrate these effects, we evaluate a simple 2D method where we pump an SM using three distinct in-plane excitation polarizations $\boldsymbol{E}_i$ and observe the corresponding emission intensities $\boldsymbol{g} = [g_1, g_2, g_3]^\dagger$ (Supplemental Section I A, Fig. S1(b)).

The normalized second moments are computed by inverting the basis matrix: $[\langle \zeta_x^2 \rangle, \langle \zeta_y^2 \rangle, \langle \zeta_x \zeta_y \rangle]^\dagger = \boldsymbol{B}_{\mathrm{ExMod}}^{-1}(\boldsymbol{g} - \boldsymbol{b})/s$. Rearranging them into a 2-by-2 Hermitian matrix $\boldsymbol{M}_{2\mathrm{D}}$ and decomposing it as

$$\boldsymbol{M}_{2\mathrm{D}} = \begin{bmatrix} \langle \zeta_x^2 \rangle & \langle \zeta_x \zeta_y \rangle \\ \langle \zeta_x \zeta_y \rangle & \langle \zeta_y^2 \rangle \end{bmatrix} = \gamma_{2D} \boldsymbol{\nu}_1 \boldsymbol{\nu}_1^\dagger + \frac{1 - \gamma_{2\mathrm{D}}}{2} \boldsymbol{I}, \quad (3)$$

we obtain the in-plane rotational constraint $\gamma_{2\mathrm{D}} = 2\lambda_1 - 1$ (Fig. S3). The scalars λ_i and vectors $\boldsymbol{\nu}_i$ represent the ith eigenvalue and eigenvector of $\boldsymbol{M}_{2\mathrm{D}}$, respectively. The matrix $\boldsymbol{M}_{2\mathrm{D}}$ can be interpreted as a superposition of a fixed dipole with orientation $\boldsymbol{\nu}_1$ and intensity fraction $\gamma_{2\mathrm{D}}$ and an isotropic emitter with intensity fraction $1 - \gamma_{2\mathrm{D}}$. The rotational constraint $\gamma_{2\mathrm{D}} = 1$ represents a completely immobile emitter, and $\gamma_{2\mathrm{D}} = 0$ represents a freely-rotating molecule. Note that $\gamma_{2\mathrm{D}}$ can be converted to an equivalent half-angle α for an SM uniformly diffusing within a cone [3], an equivalent LD, or an equivalent rotational anisotropy (Supplemental Section II D).

We assume that the measured second-order moments $\langle \hat{\zeta_i} \hat{\zeta_j} \rangle$ follow unbiased Gaussian distributions with precision achieving the Cramér-Rao lower bound (CRLB) [28]. Therefore, for a simplified case where the three excitation polarizations are symmetric and linear, i.e., $\boldsymbol{E}_1 \propto [1, 0]^\dagger$, $\boldsymbol{E}_2 \propto [-1/2, -\sqrt{3}/2]^\dagger$, $\boldsymbol{E}_3 \propto [-1/2, \sqrt{3}/2]^\dagger$, and the average orientation of the emitter lies within the xz plane, i.e., $\bar{\zeta_y} = 0$, the probability density function (PDF) of measurements of rotational constraint $\hat{\gamma}_{2\mathrm{D}}$ is given by (Supplemental Section II A)

$$p(\hat{\gamma}_{2\mathrm{D}}) = \frac{\hat{\gamma}_{2\mathrm{D}}}{4\sigma^2} \exp\left(-\frac{\hat{\gamma}_{2\mathrm{D}}^2 + \gamma_{2\mathrm{D}}^2}{8\sigma^2} \right) I_0\left(\frac{\hat{\gamma}_{2\mathrm{D}} \gamma_{2\mathrm{D}}}{4\sigma^2} \right). \quad (4)$$

The measurement precision of the second moments is $\sigma = \sigma^{\mathrm{CRLB}}_{\langle \hat{\zeta_x^2} \rangle} = \sigma^{\mathrm{CRLB}}_{\langle \hat{\zeta_x} \hat{\zeta_y} \rangle}$, $\gamma_{2\mathrm{D}}$ is the true rotational constraint of the SM, and $I_\alpha(\cdot)$ is the modified Bessel function of the first kind. This PDF matches simulated measurements using realistic noise (Fig. S4). The expectation of $\hat{\gamma}_{2\mathrm{D}}$ (Fig. 1(b)) is given by [29]

$$E(\hat{\gamma}_{2\mathrm{D}}) = \sigma \sqrt{2\pi} L_{1/2}^{(0)}\left(-\frac{\gamma_{2\mathrm{D}}^2}{8\sigma^2} \right), \quad (5)$$

where $L_n^{(\alpha)}$ is the generalized Laguerre polynomial. Critically, this expectation does not equal the true constraint $\gamma_{2\mathrm{D}}$ for any nonzero measurement precision σ.

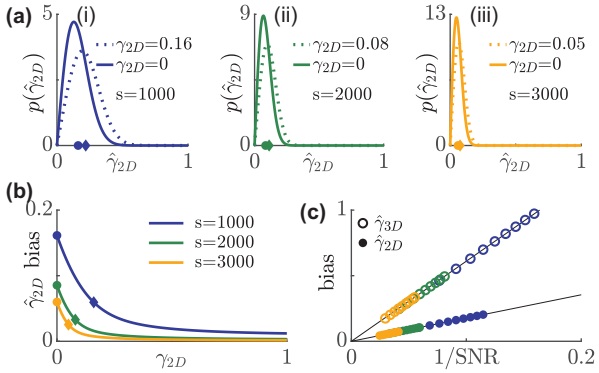

FIG. 1. Distribution and bias of rotational constraint measurements $\hat{\gamma}_{2\mathrm{D}}$ using in-plane excitation polarization modulation. (a) A non-central chi PDF describes the distribution of $\hat{\gamma}_{2\mathrm{D}}$ under $s =$ (i) 1000, (ii) 2000, and (iii) 3000 signal photons with $\mathbf{1}^\dagger \boldsymbol{b} = 7290$ background photons per 526.5×526.5 nm^2 ($3.5\times$ FWHM of a diffraction-limited spot) region. Solid line: isotropic emitters, dashed line: emitter whose bias is smaller by $1/e$ compared to an isotropic emitter. Circles and diamonds on the x axis represent the mean of the aforementioned two distributions, respectively. (b) Average bias in $\hat{\gamma}_{2\mathrm{D}}$ versus the ground truth $\gamma_{2\mathrm{D}}$. Blue, green, and orange represent 1000, 2000, and 3000 signal photons, respectively. Circles and diamonds correspond to the same data points in (a). (c) Bias in the measured rotational constraint of isotropic emitters scales linearly with the inverse of SNR, $\sqrt{s + \mathbf{1}^\dagger \boldsymbol{b}}/s$. The linearity holds for both $\hat{\gamma}_{2\mathrm{D}}$ and $\hat{\gamma}_{3\mathrm{D}}$ measured using the Tri-spot PSF under a comparable range of background photons. Solid circles: $\hat{\gamma}_{2\mathrm{D}}$, open circles: $\hat{\gamma}_{3\mathrm{D}}$.

For a typical background of 30 photons per 58.5×58.5 nm^2 (one simulated camera pixel) in an SM experiment, the expected biases $\hat{\gamma}_{2\mathrm{D}} - \gamma_{2\mathrm{D}}$ for an isotropic emitter when 1000, 2000, 3000 signal photons are detected are 0.16, 0.09, and 0.06, respectively. To provide some physical intuition, these biases correspond to half-angle errors of 13°, 7°, and 5°, respectively, if the molecule is uniformly diffusing within a cone in the xy plane. The bias decays faster with increasing constraint (decreasing cone angle) as the brightness of the emitter increases. The bias is reduced to $1/e$ times its maximum, which occurs at $\gamma_{2\mathrm{D}} = 0$, when $\gamma_{2\mathrm{D}} = 0.16, 0.08$, and 0.05 for 1000, 2000, and 3000 photons detected, respectively (Fig. 1(a),(b)).

For an isotropic emitter, g_i does not change for different excitation polarizations, and therefore, the precision of the second-moment estimates can be represented as $\sigma = \sqrt{(s + \mathbf{1}^\dagger \boldsymbol{b})/2}/s$ (Supplemental Section II A). The average apparent rotational constraint for an isotropic

emitter is therefore given by

$$E(\hat{\gamma}_{\mathrm{2D,iso}}) = \sqrt{\pi}\frac{\sqrt{s+\mathbf{1}^\dagger \boldsymbol{b}}}{s} = \frac{\sqrt{\pi}}{SNR}, \tag{6}$$

where the bias in the apparent rotational constraint scales linearly with the inverse of the signal-to-noise ratio (SNR, Fig. 1(c)).

With the relation between measurement bias, SNR, and basis-image matrix in mind, we extend our framework to measurements of 3D orientation. Similarly, we assemble a 3-by-3 second-moment matrix and decompose it as

$$\begin{aligned}\boldsymbol{M}_{\mathrm{3D}} &= \begin{bmatrix} \langle\mu_x^2\rangle & \langle\mu_x\mu_y\rangle & \langle\mu_x\mu_z\rangle \\ \langle\mu_x\mu_y\rangle & \langle\mu_y^2\rangle & \langle\mu_y\mu_z\rangle \\ \langle\mu_x\mu_z\rangle & \langle\mu_y\mu_z\rangle & \langle\mu_z^2\rangle \end{bmatrix} = \gamma_{\mathrm{3D}}\boldsymbol{\nu}_1\boldsymbol{\nu}_1^\dagger \\ &+ \tfrac{(1-\gamma_{\mathrm{3D}})}{3}\boldsymbol{I} + \tfrac{\lambda_2-\lambda_3}{2}\left(\boldsymbol{\nu}_2\boldsymbol{\nu}_2^\dagger - \boldsymbol{\nu}_3\boldsymbol{\nu}_3^\dagger\right), \end{aligned} \tag{7}$$

where the 3D rotational constraint $\gamma_{\mathrm{3D}} = (3\lambda_1 - 1)/2$. If the molecule's rotational diffusion is symmetric around a certain average orientation, then the smaller eigenvalues λ_2 and λ_3 are identical due to symmetry. Similarly, the matrix $\boldsymbol{M}_{\mathrm{3D}}$ can be viewed as a superposition of a fixed dipole and an isotropic emitter, plus a nuisance term that is orthogonal to $\boldsymbol{\nu}_1$. This nuisance term can arise from either photon shot noise or asymmetric rotation. In contrast to the case of 2D excitation modulation, the eigenvalues of the measured second-moment matrix $\hat{\boldsymbol{M}}_{\mathrm{3D}}$ do not have a closed-form distribution. We therefore perform Monte Carlo simulations on isotropic emitters imaged using the Tri-spot point spread function (PSF) [30] (Fig. S1(c)). The linear relation between the bias in $\hat{\gamma}_{\mathrm{3D}}$ and the inverse of SNR still approximately holds (Fig. 1(c)).

Although both in-plane γ_{2D} (Eq. (3)) and 3D γ_{3D} (Eq. (7)) rotational constraints have identical interpretations for limiting cases, e.g., $\gamma_{\mathrm{2D}} = \gamma_{\mathrm{3D}} = 0$ represents a rotationally free emitter and $\gamma_{\mathrm{2D}} = \gamma_{\mathrm{3D}} = 1$ represents a completely immobile emitter, these two quantities *may differ* for any *partially-constrained* dipole emitter. As is well-known when measuring translational dynamics in 2D and 3D, identical 3D orientation trajectories can produce different rotational diffusion measurements in 2D versus 3D. The relationship between these measurements must be considered carefully when evaluating the best technique for a given target. Here, we consider a symmetrically-rotating molecule in 3D and assemble $\boldsymbol{M}_{\mathrm{2D}}$ using a subset of elements from $\boldsymbol{M}_{\mathrm{3D}}$:

$$\boldsymbol{M}_{\mathrm{2D}} = \frac{\begin{bmatrix} 3\bar{\mu}_x^2 - 1 + 1/\gamma_{\mathrm{3D}} & 3\bar{\mu}_x\bar{\mu}_y \\ 3\bar{\mu}_x\bar{\mu}_y & 3\bar{\mu}_y^2 - 1 + 1/\gamma_{\mathrm{3D}} \end{bmatrix}}{1 - 3\bar{\mu}_z^2 + 2/\gamma_{\mathrm{3D}}}, \tag{8}$$

where $[\bar{\mu}_x, \bar{\mu}_y, \bar{\mu}_z]^\dagger = \boldsymbol{\nu}_1$ is the average orientation of the dipole emitter. The in-plane rotational constraint γ_{2D} is now given by (Supplemental Section II B)

$$\gamma_{\mathrm{2D}} = \frac{3(1-\bar{\mu}_z^2)}{1 - 3\bar{\mu}_z^2 + 2/\gamma_{\mathrm{3D}}}. \tag{9}$$

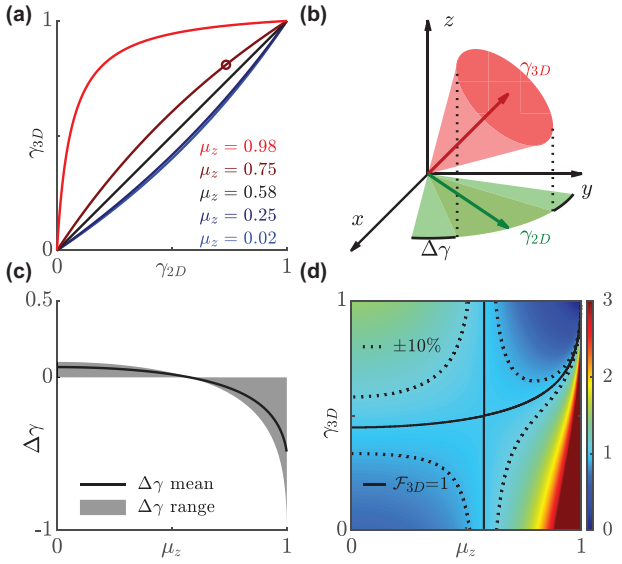

FIG. 2. Comparison of in-plane γ_{2D} and 3D γ_{3D} rotational constraints. (a) The relation between γ_{2D} and γ_{3D} varies with the average orientation along the z axis, $\bar{\mu}_z$ (Eq. 9). Black line corresponds to $\bar{\mu}_z = \sqrt{1/3} \approx \cos 54.7°$ so that $\gamma_{\mathrm{2D}} = \gamma_{\mathrm{3D}}$. (b) A dipole emitter with an out-of-plane orientation $\bar{\mu}_z = 0.75$ that has $\gamma_{\mathrm{3D}} = 0.81$ (a cone half-angle of 30°, open circle in (a)) appears to be more rotationally free in the xy plane ($\gamma_{\mathrm{2D}} = 0.73$, cone half-angle of 38°). (c) The mean difference $\Delta\gamma$ across all 3D orientation space ranges from -1 to 0.06. Solid line represents the average across all possible values of γ_{3D}, and the shaded region represents the range of the difference. (d) 3D enhancement factor $\mathcal{F}_{\mathrm{3D}}$ as a function of γ_{3D} and $\bar{\mu}_z$. Solid line represents the equilibrium point where in-plane and 3D rotational constraints measure changes in rotational dynamics with equal sensitivity. Dashed line represents a ±10% difference in sensitivity.

The 2D and 3D rotational constraints are identical for a molecule exhibiting an average out-of-plane component of $\bar{\mu}_z^2 = 1/3$ (corresponding to a "magic" polar angle $\approx 54.7°$, Fig. 2a). Note that γ_{2D} depends on *both* the 3D rotational constraint γ_{3D} and average out-of-plane orientation $\bar{\mu}_z$; in-plane orientation measurement methods are only sensitive to γ_{2D} and must incorporate prior knowledge of $\bar{\mu}_z$ in order to compute an equivalent 3D rotational constraint γ_{3D}. The average difference in constraint $\Delta\gamma = \gamma_{\mathrm{2D}} - \gamma_{\mathrm{3D}}$ (Fig. 2(c)) is within ±0.1 for $\bar{\mu}_z <= 0.8$, indicating that both γ_{2D} and γ_{3D} quantify the rotational dynamics of a dipole emitter similarly as long as the out-of-plane component is small. However, for a molecule that is almost along the optical axis, e.g. $\bar{\mu}_z = 0.98$ or polar angle = 11°, $|\Delta\gamma|$ can be as large as 0.61; a highly-constrained molecule in 3D ($\gamma_{\mathrm{3D}} = 0.80$ or

a cone half-angle of 30°) appears to be almost completely unconstrained using an in-plane measurement method ($\gamma_{2D} = 0.20$ or a cone half-angle of 75°). This interdependence of μ_z, γ_{2D}, and γ_{3D} has important implications for orientation-measurement techniques. If a technique cannot measure all six second-moments in 3D directly, then one must use a prior assumption on the out-of-plane orientation to calculate the rotational constraint (or vice versa). Any errors in this assumption can dramatically impact measurement accuracy.

A natural consequence of using in-plane versus 3D orientation measurements is that these techniques have different sensitivities for measuring changes in rotational dynamics. One may evaluate sensitivity by computing the standard deviation of rotational constraint estimates given a certain noise level. However, this approach ignores our observation that a three-dimensional technique and an in-plane technique, even with the same measurement precision, will quantify a change in γ_{3D} differently depending on μ_z. Here, we quantify the enhancement factor $\mathcal{F}_{3D}$ as the ratio of partial derivatives of γ_{3D} to γ_{2D} (Fig. 2(d)):

$$\mathcal{F}_{3D} = \frac{\partial \gamma_{3D}}{\partial \gamma_{2D}} = \frac{\left(\gamma_{3D}(1-3\bar{\mu}_z^2)+2\right)^2}{6(1-\bar{\mu}_z^2)}. \tag{10}$$

An enhancement factor $\mathcal{F}_{3D}$ greater than one implies that a given change in $\hat{\gamma}_{3D}$ maps to a smaller change in $\hat{\gamma}_{2D}$, i.e., for the same measurement uncertainty, it is easier to detect a change in $\hat{\gamma}_{3D}$ than $\hat{\gamma}_{2D}$. The sensitivity of the in-plane measurement to a change in rotational constraint highly depends on the out-of-plane component of molecular orientation. For example, for the aforementioned molecule with $\bar{\mu}_z = 0.98$, an in-plane technique is especially insensitive to changes in rotational motion for most values of γ_{3D}. However, when the molecule is almost immobile, the in-plane method becomes very sensitive, i.e., a small change in γ_{3D} produces a large, easily-detectable change in $\hat{\gamma}_{2D}$.

To provide quantitative metrics for choosing the optimal orientation measurement technique, we compare multiple popular and state-of-the-art methods. We first consider an ideal 3D (6×6) basis-image matrix

$$\boldsymbol{B}_{\text{ideal}} = \frac{1}{2}\begin{bmatrix} \boldsymbol{I}_3 & \boldsymbol{I}_3 \\ \boldsymbol{I}_3 & -\boldsymbol{I}_3 \end{bmatrix}, \tag{11}$$

such that each column of $\boldsymbol{B}_{\text{ideal}}$ is orthogonal and has identical energy. The precision of second-moment measurements can be calculated as $\sigma^{\text{CRLB}}_{\langle \mu_i \mu_j \rangle} = \sqrt{(s + \mathbf{1}^\dagger \boldsymbol{b})/3}/s$ (Supplemental Section II B). Therefore, the average apparent 3D rotational constraint for an isotropic emitter is given by

$$E(\hat{\gamma}_{3D,\text{iso}}) = \frac{\eta\sqrt{3}}{2}\frac{\sqrt{s+\mathbf{1}^\dagger \boldsymbol{b}}}{s} = \frac{\eta\sqrt{3}}{2\,SNR}, \tag{12}$$

where $\eta \approx 1.848$ is the expectation of the largest eigenvalue of a Hermitian random matrix $\boldsymbol{H}$ whose elements

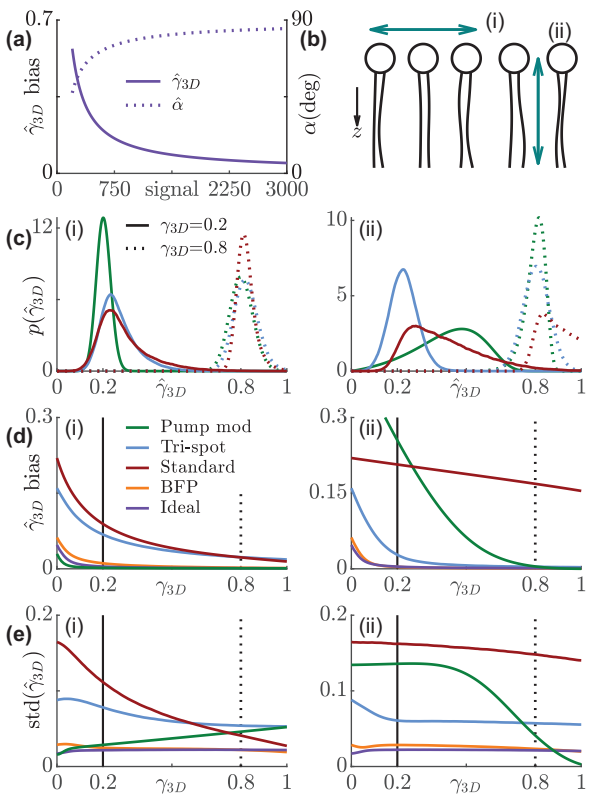

FIG. 3. Bias and precision of rotational constraint measurements using various techniques. (a) Minimum detectable rotational constraint for various numbers of signal photons and 4860 total background photons. Solid line represents the expectation of measured rotational constraint $\hat{\gamma}_{3D}$ for isotropic emitters; dashed line represents the corresponding cone half-angle $\hat{\alpha}$ if the molecule is symmetrically diffusing in a cone. (b) Concept of (i) a horizontally- and (ii) a vertically-orientated fluorescent molecule within a lipid membrane. (c) The distribution of 3D rotational constraint estimates $\hat{\gamma}_{3D}$ computed using a non-central chi PDF for in-plane excitation modulation and Monte Carlo simulations for the Tri-spot and standard PSF. Solid line: true rotational constraint $\gamma_{3D} = 0.2$ (cone half-angle $\alpha = 72°$); dashed line: $\gamma_{3D} = 0.8$ ($\alpha = 31°$). (d) Bias and (e) standard deviation are evaluated for all aforementioned, back focal plane, and ideal imaging techniques. Green: in-plane excitation modulation, blue: Tri-spot PSF, red: standard PSF, orange: back focal plane imaging, purple: ideal basis-image matrix.

H_{ij} are i.i.d. standard normal random variables for $i \geq j$. The imaging system represented by $\boldsymbol{B}_{\text{ideal}}$ separates the six second-moments into independent measurements with ideal collection efficiency and, thus, represents a fundamental limit on the measurement accuracy of 3D rotational constraint. That is, for a finite SNR, the emission pattern of a freely-rotating molecule would appear to be identical to that of a partially-fixed emitter using any 3D orientation measurement method, and the apparent constraint is always greater than or equal to the result in Eq. (12). To provide some physical intuition (Fig. 3(a)),

for 1000 signal photons and 10 background photons per pixel detected, the expectation of $\hat{\gamma}_{3D}$ is 0.12, meaning that a SM diffusing within a cone of half-angle $\alpha = 78°$ would be indistinguishable from a rotationally-free SM ($\alpha = 90°$).

Besides the aforementioned ideal, Tri-spot, and in-plane excitation methods, we also analyze the performance of fitting fine features of the standard PSF [31] and direct imaging of the back focal plane (BFP) [24] (Fig. S1(d,e)). Due to the lack of sensitivity in measuring $\langle \mu_x \mu_z \rangle$ and $\langle \mu_y \mu_z \rangle$ using the standard PSF, only three second moments were used to compute rotational constraint (Supplemental Section II C).

We simulated two limiting cases, mimicking two orientations of fluorescent dye molecules embedded within a lipid membrane [32] (Fig. 3(b)), where the average orientation is almost perpendicular (Fig. 3(i), $\bar{\mu}_z = 0.02$, polar angle = 89°) and almost parallel (Fig. 3(ii), $\bar{\mu}_z = 0.98$) to the optical axis. The simulated SNR for all the methods is 3000 signal photons to 20 total background photons per pixel per unit time (Supplemental Section I E).

The Tri-spot PSF and BFP imaging have similar performance for both in-plane and out-of-plane molecules due to their relatively uniform sensitivity measuring all orientational second-order moments. The in-plane excitation method, as expected, exhibits high accuracy and precision for in-plane molecules. Its bias in $\hat{\gamma}_{3D}$ is even lower than the ideal 3D technique because of the improved SNR of distributing an SM's photons over 2× fewer measurements. For out-of-plane molecules, its bias and standard deviation are much worse compared to 3D methods except when the rotational constraint is sufficiently high. The standard PSF, due to the lack of sensitivity towards two of the out-of-plane second-order moments, also exhibits a large bias and standard deviation for out-of-plane molecules. However, it has better performance for measuring the rotational motion of highly constrained in-plane molecules than both the Tri-spot PSF and excitation modulation. This implies that a method specifically designed for measuring a subset of, instead of all six (3D), orientational second moments can provide superior measurement precision under certain experimental conditions.

In summary, we analyzed the fundamental bias in measurements of rotational dynamics caused by finite SNR. We derived a lower bound on this bias, that is, no method can detect a rotational constraint smaller than this bound. While we defined rotational constraint in terms of the eigenvalues of a matrix composed of second moments of $\boldsymbol{\mu}$, any parameterization of SM rotational diffusion, e.g., fluorescence anisotropy [33], will also suffer bias since any measurement will capture a finite number of photons (Supplemental Section II D). Our framework is easily adaptable for characterizing the bias of any orientation-measurement method via calculation of the basis images $\boldsymbol{B}_{ij}$. We show that there is a complex relationship between in-plane and 3D molecular orientation, such that a molecule's 2D rotational constraint can appear significantly smaller or larger than its true constraint in 3D. Using our framework, we compared multiple methods for measuring rotational dynamics, revealing how the accuracy and precision of these measurements vary for in-plane and out-of-plane SMs. In particular, our results show that 3D methods are particularly important for quantifying accurately the rotational dynamics of molecules with significant out-of-plane orientations. Our framework should be useful for choosing between existing methods and optimizing new techniques that achieve maximum accuracy and precision in various imaging scenarios.

This work was supported by the National Science Foundation under grant number ECCS-1653777 and by the National Institute of General Medical Sciences of the National Institutes of Health under grant number R35GM124858.

* mdlew@wustl.edu

[1] T. Ha, T. Enderle, D. S. Chemla, P. R. Selvin, and S. Weiss, Physical Review Letters **77**, 3979 (1996).
[2] T. Ha, J. Glass, T. Enderle, D. S. Chemla, and S. Weiss, Physical Review Letters **80**, 2093 (1998).
[3] A. S. Backer, M. Y. Lee, and W. E. Moerner, Optica **3**, 659 (2016).
[4] H. Sosa, E. J. G. Peterman, W. E. Moerner, and L. S. B. Goldstein, Nature Structural Biology **8**, 540 (2001).
[5] E. J. Peterman, H. Sosa, L. S. Goldstein, and W. Moerner, Biophysical Journal **81**, 2851 (2001).
[6] J. N. Forkey, M. E. Quinlan, M. A. Shaw, J. E. T. Corrie, and Y. E. Goldman, Nature **422**, 399 (2003).
[7] J. F. Beausang, D. Y. Shroder, P. C. Nelson, and Y. E. Goldman, Biophysical Journal **104**, 1263 (2013).
[8] L. G. Lippert, T. Dadosh, J. A. Hadden, V. Karnawat, B. T. Diroll, C. B. Murray, E. L. F. Holzbaur, K. Schulten, S. L. Reck-Peterson, and Y. E. Goldman, Proceedings of the National Academy of Sciences **114**, E4564 (2017)
[9] J. Engelhardt, J. Keller, P. Hoyer, M. Reuss, T. Staudt, and S. W. Hell, Nano Letters **11**, 209 (2011).
[10] M. P. Backlund, M. D. Lew, A. S. Backer, S. J. Sahl, G. Grover, A. Agrawal, R. Piestun, and W. E. Moerner, Proceedings of the National Academy of Sciences **109**, 19087 (2012).
[11] M. D. Lew, M. P. Backlund, and W. E. Moerner, Nano Letters **13**, 3967 (2013).
[12] M. D. Lew and W. E. Moerner, Nano Letters **14**, 6407 (2014).
[13] M. P. Backlund, M. D. Lew, A. S. Backer, S. J. Sahl, and W. E. Moerner, ChemPhysChem **15**, 587 (2014).
[14] P. L. Edmiston, J. E. Lee, L. L. Wood, and S. S. Saavedra, The Journal of Physical Chemistry **100**, 775 (1996).
[15] J. T. Fourkas, Optics Letters **26**, 211 (2001).
[16] R. K. Benninger, B. Önfelt, M. A. Neil, D. M. Davis, and P. M. French, Biophysical Journal **88**, 609 (2005).
[17] G. Steinbach, I. Pomozi, O. Zsiros, A. Páy, G. V. Horváth, and G. Garab,

Cytometry Part A **73A**, 202 (2008).
[18] A. J. Berglund, Physical Review E **82**, 011917 (2010).
[19] Y. Wong, Z. Lin, and R. J. Ober, IEEE Transactions on Signal Processing **59**, 895 (2011).
[20] X. Michalet and A. J. Berglund, Physical Review E **85**, 061916 (2012).
[21] M. P. Backlund, R. Joyner, and W. E. Moerner, Physical Review E **91**, 062716 (2015).
[22] C. P. Calderon, Physical Review E **93**, 053303 (2016).
[23] M. Böhmer and J. Enderlein, Journal of the Optical Society of America B **20**, 554 (2003).
[24] M. A. Lieb, J. M. Zavislan, and L. Novotny, Journal of the Optical Society of America B **21**, 1210 (2004)
[25] D. Axelrod, Journal of Microscopy **247**, 147 (2012).
[26] A. S. Backer and W. E. Moerner, The Journal of Physical Chemistry B **118**, 8313 (2014).
[27] A. S. Backer and W. E. Moerner, Optics Express **23**, 4255 (2015).
[28] T. K. Moon and W. C. Stirling, *Mathematical methods and algorithms for signal processing* (Prentice hall Upper Saddle River, NJ, 2000).
[29] A. Nuttall, IEEE Transactions on Information Theory **21**, 95 (1975).
[30] O. Zhang, J. Lu, T. Ding, and M. D. Lew, Applied Physics Letters **113**, 031103 (2018).
[31] K. I. Mortensen, L. S. Churchman, J. A. Spudich, and H. Flyvbjerg, Nature Methods **7**, 377 (2010).
[32] T. Motegi, H. Nabika, and K. Murakoshi, Physical Chemistry Chemical Physics **15**, 12895 (2013).
[33] J. R. Lakowicz, *Principles of Fluorescence Spectroscopy* (Kluwer Academic/Plenum Publishers, New York, 2004).